Materials Transactions, Vol. 62, No. 2 (2021) pp. 167 to 176
©2020 The Japan Institute of Metals and Materials

In Situ Synchrotron X-ray Analysis: Application of High-Pressure Sliding Process to Ti Allotropic Transformation

Zenji Horita[1,2,3,4,*], Daisuke Maruno[4], Yukimasa Ikeda[4], Takahiro Masuda[4,5], Yongpeng Tang[1,4], Makoto Arita[4], Yuji Higo[6], Yoshinori Tange[6] and Yasuo Ohishi[6]

[1]*Graduate School of Engineering, Kyushu Institute of Technology, Kitakyushu 804-8550, Japan*
[2]*Magnesium Research Center, Kumamoto University, Kumamoto 860-8555, Japan*
[3]*Synchrotron Light Application Center, Saga University, Saga 840-8502, Japan*
[4]*Department of Materials Science and Engineering, Kyushu University, Fukuoka 819-0395, Japan*
[5]*Department of Mechanical Engineering and Materials Science, Yokohama National University, Yokohama 240-8501, Japan*
[6]*Japan Synchrotron Radiation Research Institute, Hyogo 679-5198, Japan*

In this study, severe plastic deformation through high-pressure sliding (HPS) was applied for *in situ* high-energy X-ray diffraction analysis at SPring-8 in JASRI (Japan Synchrotron Radiation Research Institute). Allotropic transformation of pure Ti was examined in terms of temperatures, pressures and imposed strain using a miniaturized HPS facility. The true pressure applied on the sample was estimated from the peak shift. Peak broadening due to local variation of pressure was reduced using white X-rays. The phase transformation from α phase to ω phase occurred at a pressure of ~4.5 GPa. Straining by the HPS processing was effective to promote the transformation to the ω phase and to maintain the ω phase even at ambient pressure. The reverse transformation from ω phase to α phase occurred at a temperature of ~110°C under ambient pressure, while under higher pressure as ~4 GPa, the ω phase remained stable even at ~170°C covered in this study. It was suggested that the reverse transformation from the ω phase to the α phase is controlled by thermal energy. [doi:10.2320/matertrans.MT-M2020314]

(Received October 1, 2020; Accepted November 17, 2020; Published December 25, 2020)

Keywords: *severe plastic deformation, high-pressure sliding, pure Ti, allotropic phase transformation, in situ X-ray diffraction analysis, synchrotron radiation*

1. Introduction

Recently, it was documented in a special issue of *Materials Transactions*[1,2] that mechanical and functional properties are significantly improved by imposing intense strain through severe plastic deformation (SPD). The application of the SPD process was mostly to metallic materials as found in many review papers[3–12] but, if the process is operated under high pressure using the method called high-pressure torsion (HPT),[13,14] the application is extended to less ductile and hard-to-deform materials[15–18] including intermetallics[19,20] semiconductors[3,21–24] and ceramics.[25,26] Consolidations of powders, chips and layers are also possible with the process of HPT so that the application is further extended to synthesis of bulk materials.[27–51] It is also possible to utilize high-pressure phases to produce functionalities.[50–54]

The HPT process was pioneered by Bridgman in the early 1900s,[13,14] where a disk sample is placed between upper and lower anvils and intense shear strain is introduced by rotating one anvil with respect to the other under high pressure. The Bridgman's idea of the rotation was recently modified to reciprocation of the anvils as illustrated in Fig. 1[55] so that intense shear strain was introduced to a rectangular sheet sample with the same principle as the HPT process. This process is called high-pressure sliding (HPS)[55] and applied to many metallic materials[56–59] including powder consolidation.[60] It was shown that this HPS process was applicable to rods[61–64] and pipes.[65] Furthermore, it was combined with sample feeding so that the SPD-processed area is upsized.[66,67] Such developments were intended for practical applications of the SPD process as described in a recent overview paper.[68] In this study, the HPS process is rather downsized for *in situ* X-ray analysis in a synchrotron facility during operation under high pressures and elevated temperatures.

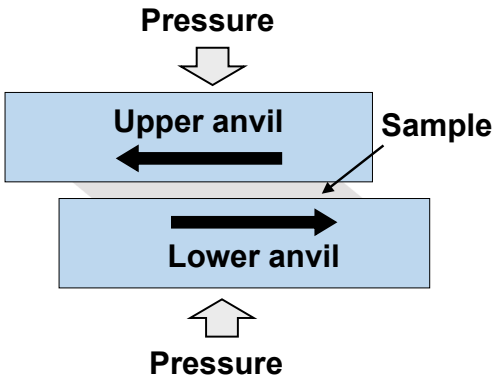

Fig. 1 Principle of high-pressure sliding (HPS).

The property improvement using the HPT and HPS processes is attributed to a high density of lattice defects generated during the processes.[69–71] Microstructural analyses are then indispensable for understanding the roles of the lattice defects and for clarifying the mechanisms involved in the improvement of the properties. In particular, *in situ* analysis is required at elevated temperature and/or high pressure as the structures may changes during heating and/or cooling the temperature, during loading and/or unloading the pressure, and during straining by the HPT and HPS processes.

In situ X-ray analyses under high pressures and high temperatures are often conducted with diamond anvil cells (DAC)[72–74] or multi anvil setups.[75,76] They are mostly used

*Corresponding author, E-mail: horita.zenji.688@m.kyushu-u.ac.jp

in hydrostatic conditions, but for the case of DAC, plastic deformation was intentionally introduced by rotation of one diamond anvil to the other, following the Bridgman's idea,[13] Blank and co-workers are the first to generate shear strain using DAC,[77,78] and extensive studies with straining by DAC were carried out by Levitas and coworkers[79] and most recently by Nomura *et al.*[80] For the case of multi anvil setup, two differential rams were incorporated in the upper and lower guide flames so that generation of plastic strain up to 30% was feasible.[81,82] Plastic strain was also introduced using a rotational Drickamer apparatus for the *in situ* examination, which were designed to examine creep behavior of geological materials under high pressures and high temperatures,[83–87] with a basic principle involved in the Bridgman's idea.[13] There was an attempt[88] where a direct illumination of high-energy X-ray was made on steel anvils for HPT while a Cu sample in the anvils was being processed by the HPT, but the analysis required deconvolution of the Cu signal, due to overlapping, from the signals emanated from the anvils.

In this study, we examine a transformation behavior of pure Ti using the HPS process developed for *in situ* high-energy X-ray analysis under high pressures and elevated temperatures. According to the temperature-pressure phase diagram in Fig. 2,[89] Ti is stable in α phase with a hexagonal close-packed (hcp) structure at ambient condition, and transforms to a simple hexagonal ω phase under a high pressure. This allotropic phase transformation was well recognized by Bridgman[90] and confirmed by Jamieson,[91] and now many reports are available for this phase transformation including reverse transformation from ω phase to α phase.[92–107]

The objective of this study is two fold: first, an *in situ* XRD analysis under high pressures and elevated temperatures is developed using the process of HPS for the first time and second, the transformation behavior of pure Ti is examined in terms of temperature, pressure and straining.

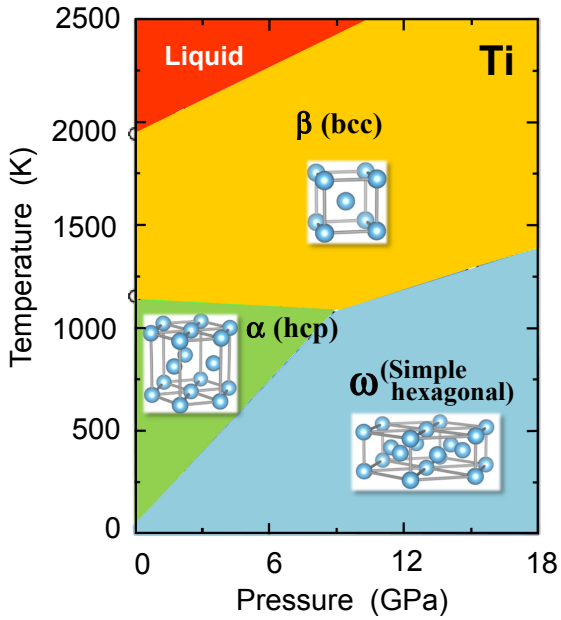

Fig. 2 Temperature-pressure phase diagram of pure Ti reproduced from Hennig *et al.*[89]

2. Experimental

2.1 HPS facility for *in situ* X-ray analysis

Figure 3 illustrates (a) a cross sectional view and (b) a plan view of an HPS assembly for *in situ* X-ray analysis. The assembly consists of upper and lower tool-steel blocks

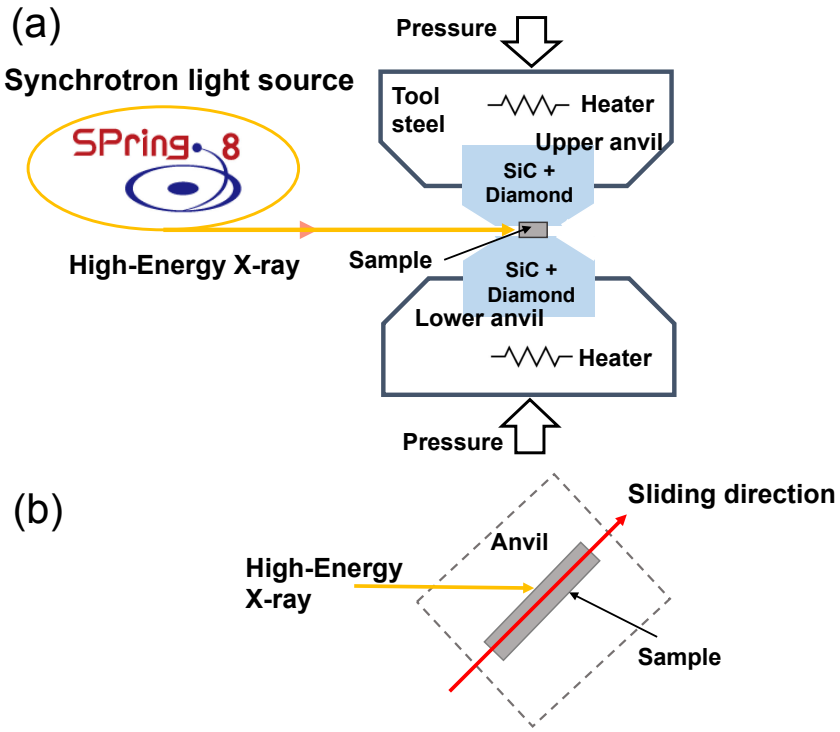

Fig. 3 Schematic illustration of *in situ* high-energy X-ray analysis using HPS process: (a) cross-sectional view and (b) plan view.

containing heaters capable of heating up to 200°C. A ceramics anvil with 10 mm cube made of a compound with SiC and diamond powders was embedded in each of the tool-steel block as illustrated in Fig. 3(a). A groove with 1 mm width and 0.2 mm depth was made across the center on one side of the cube for holding a strip sample under a semi-constrained condition. Strain was introduced by sliding the lower anvil with respect to the upper anvil with a speed 0.1 mm/s for 1 mm under a maximum load up to 60 kN. The sliding was made towards the direction at 45 degrees from the incident beam direction. An equivalent strain of ~2 is introduced through this process.

2.2 *In situ* X-ray analysis using HPS facility

In situ X-ray diffraction (XRD) analysis was carried out at BL04B1 of SPring-8 in JASRI. The HPS-processing unit described in Fig. 3 was set on guide blocks in the pressure application system named SPEED-Mk.II installed in the BL04B1 X-ray hutch.[108] The HPS unit was used with the pressure and stage controls while replacing a multi anvil setup originally set in the SPEED-Mk.II. A schematic illustration for the *in situ* X-ray analysis is shown in Fig. 4(a) and (b) for the cases of monochromatic and white X-rays, respectively.

For the former case, a strip sample with dimensions of $1 \times 7 \times 0.5\,mm^3$ was placed between the anvils and was illuminated with a beam energy of 60 keV. The area of the X-ray illumination was selected to be $0.2 \times 0.2\,mm^2$ and X-ray diffraction was recorded for a duration of 1 min. by a CCD (Charge-Coupled Device) camera. The diffraction images were then processed such that the diffracted intensities were integrated around the incident beam direction at the equal distance (i.e. at the equal angle) from the center of the image. The intensity profile was then depicted as a function of the diffraction angle. The camera length was determined by acquiring X-rays using ceria (CeO_2) particles.

For the latter case, white X-rays with beam energies of 20–150 keV were used, and only the X-rays diffracted at the mid width of the strip sample was collected using a collimator and detected by an energy dispersive Ge-type solid state detector (Ge-SSD). The collimator and the detector were located along the direction at an angle of 6 degrees from the incident beam direction. X-ray acquisition was continued for 3 min. and X-ray signals for those fulfilled the diffraction conditions were recorded as a function of X-ray energy.

2.3 Sample preparation

A pure Ti sheet (99.94%) with a thickness of 1 mm was cut into strips with dimensions of $1 \times 7 \times 0.5\,mm^3$ and they were annealed at 800°C for 1 hour in vacuum in order to examine the transformation behaviour from α phase to ω phase. For the examination of the reverse transformation from ω phase to α phase, the pure Ti sheet was also cut into disks with a diameter of 10 mm. All disks were annealed at 800°C for 1 hour in vacuum and were processed by HPT at room temperature under a pressure of 6 GPa through 4 turns with a rotation speed of 0.25 r.p.m as described before.[99,107] For *in situ* X-ray diffraction (XRD) analysis, strip samples with dimensions of $1 \times 7 \times 0.5\,mm^3$ were cut from the portion far away from the disk center. Each strip was placed in a groove for the analysis as illustrated in Fig. 3 and Fig. 4.

2.4 Microstructural analysis

For transmission electron microscopy (TEM), the strip samples after HPS processing were cut to 3 mm lengths at the center parts and were mechanically ground to thicknesses of 0.15 mm. They were further thinned for TEM using a twin-jet electrochemical apparatus in a solution of 70%CH_3OH,

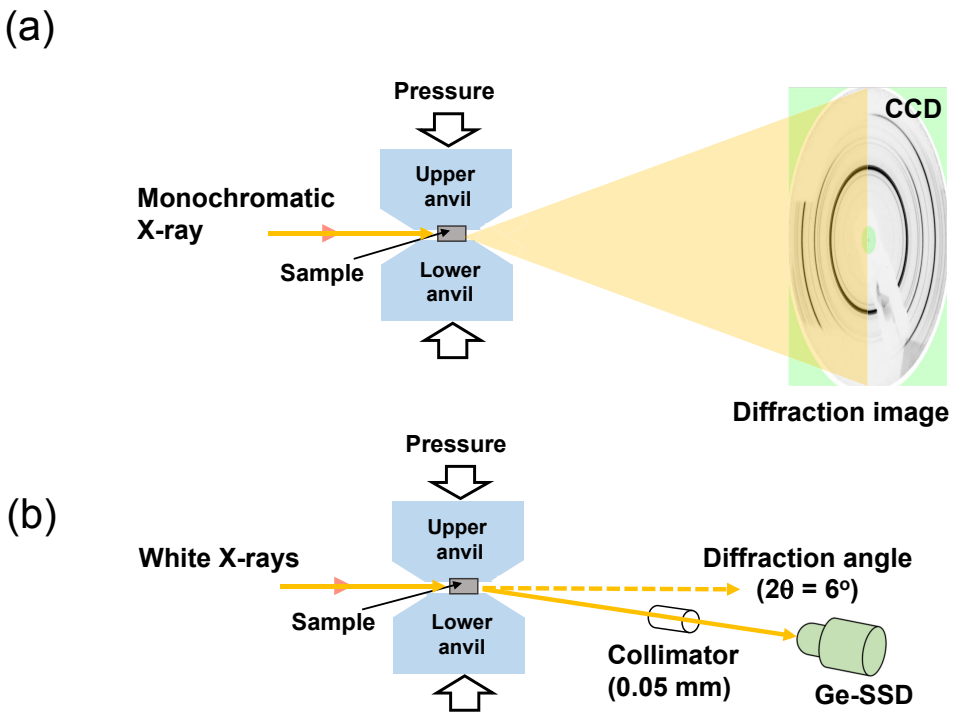

Fig. 4 Schematic illustration of *in situ* high-energy X-ray analysis using HPS process: (a) for monochromatic X-ray and (b) for white X-rays.

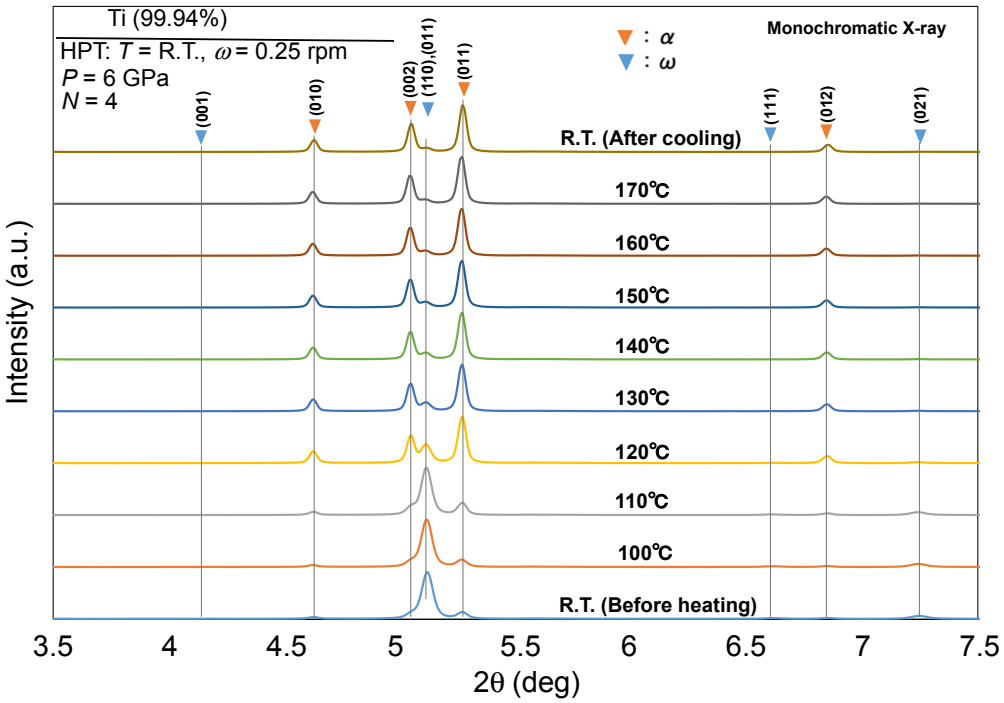

Fig. 5 X-ray profiles for HPT-processed sample before heating, during heating to 170°C and after cooling to room temperature.

25%$CH_3(CH_2)_3CCH_2CH_2OH$ and 5%$HClO_4$ under a voltage of 10–20 V. Microstructures were observed using a Hitachi H-8100 transmission electron microscope at an accelerating voltage of 200 kV.

3. Results

3.1 Transformation behaviour during heating under ambient pressure and higher pressure

Figure 5 shows X-ray profiles for samples at the as-HPT-processed state before heating and at the states during temperature increase to 170°C including the state after cooling to room temperature. The sample at the as-HPT-processed state contains a large fraction of the ω phase. This ω phase peaks decrease as the temperature increases. The transformation to α phase began to occur at ~110°C. The transformation further proceeded until the temperature reached ~140°C, and little fraction of the ω phase remained after heating up to ~170°C.

The transformation behavior under loading of 50 kN (corresponding to a nominal pressure of 7 GPa) is shown in Fig. 6. It is found that the behavior is clearly different from the one under ambient pressure in Fig. 5. The fraction of the ω phase remained unchanged even after heating up to ~170°C. The presence of the ω phase was also confirmed after cooling to room temperature and after releasing the pressure (unloading). The peak shift occurred because of the application of the pressure. Close analysis revealed that the real pressure applied on the sample was ~4 GPa as discussed later. It should be noted that diamond (111) peaks are visible in the X-ray profiles and this is because the space between the upper and lower anvils was reduced due to the loading so that the X-ray now illuminated on the sample together with the anvils. It should be also noted that the presence of the β phase was not expected for the conditions of pressure and temperature adopted in this study based on the first-principle calculation reported earlier.[102)]

3.2 Effect of straining under high pressure

Intense strain was introduced under three different nominal pressures, 6, 7 and 8.5 GPa, and the corresponding X-ray profiles are shown in Fig. 7(a)–(c), respectively. Each includes the X-ray profiles before and after application of pressure (loading), after straining by HPS processing and after releasing the pressure (unloading) following the HPS processing. It should be noted that the samples used for this examination were the strips subjected to annealing at 800°C for 1 h in an evacuated tube after extracting from the as-received pure Ti sheet. Thus, only the peaks from the α phase are visible in all the profiles before loading. Besides the peak shift due to the application of high pressure, no peak from ω phase appears after HPS processing under 6 GPa. The peaks corresponding to the ω phase appear after applications of 7 and 8.5 GPa. For the application of 7 GPa, the transformation to the ω phase appreciably occurs after straining by the HPS processing. For the application of 8.5 GPa, the transformation further occurs after loading to 8.5 GPa, and it is more pronounced after straining by the HPS processing. The ω phase peaks after releasing the pressures are still visible. This suggests that straining is effective for the transformation to the ω phase.

White X-rays were further used instead of the monochromatic X-ray to examine the effect of straining under high pressures. The X-ray profiles are then shown in Fig. 8(a)–(c) as a function of the X-ray energy for the nominal pressures of 6, 7 and 8.5 GPa, respectively. When compared with the ones acquired with monochromatic X-rays shown in Fig. 7(a)–(c), it is found that the peak broadening is well reduced. Nevertheless, the trend observed in Fig. 7 well holds: no ω phase after the application of 6 GPa and after straining by

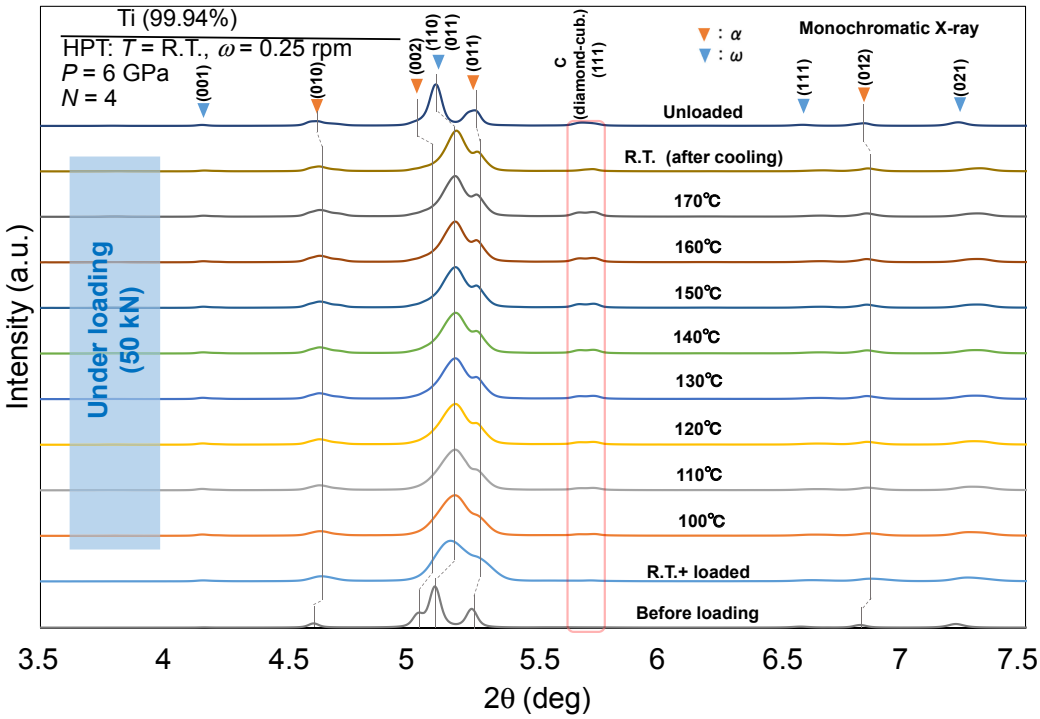

Fig. 6 X-ray profiles under loading of 50 kN (nominal pressure of 7 GPa) for HPT-processed sample before heating, during heating to 170°C and after cooling to room temperature. X-ray profiles before loading and after loading are also included.

the HPS processing, but it forms after the application of 7 GPa and more appreciably after further straining by the HPS processing under 7 GPa. The formation of the ω phase is marked when the pressure is applied and the HPS processing is operated under 8.5 GPa. The ω phase remained after unloading from both 7 and 8.5 GPa. It should be noted that diamond (111) + SiC (012) peaks appeared in the X-ray profiles upon application of loads and after straining by HPS processing. As commented in association with Fig. 6, this is because the space between the upper and lower anvils was reduced due to the loading and straining so that the illumination of the X-ray included a part of the anvils.

3.3 Microstructures after strained by HPS

Microstructures observed by TEM after HPS processing under nominal pressures of 6 and 8.5 GPa are shown in Fig. 9(a) and (b), respectively, where bright-filed images are given on the left and dark-field images are on the right. Selected area electron diffraction (SAED) patterns are at the center with the diffraction spots indicated by the arrows for the dark-field images. The grain sizes measured from the dark-field images are ~250 and ~110 nm, respectively. The grain boundaries are not well defined, which are typical of the samples subjected to SPD process. The misorientation angle may not be sufficiently large but ultrafine-grained structures are well developed as expected from SPD processing. It should be noted that the bright areas in the dark field image in Fig. 9(a) correspond to the α phase based on the X-ray profiles in Fig. 8(a). However, the identification is not possible for those in Fig. 9(b) because the diffracted beams of (002) and (011) for the α phase and of (110) and (011) for the ω phase are too close to each other to distinguish due to insufficient resolution in the diffraction pattern.

4. Discussion

According to the temperature-pressure phase diagram shown in Fig. 2,[89] the pressure of 6 GPa at ambient temperature are within the region where the ω phase is stable. However, no ω phase was detected in the X-ray profiles as shown in Fig. 7(a) and Fig. 8(a). In order to make a rigorous evaluation, it is necessary to estimate the true pressure applied on the strip sample. It is more likely that the pressure should be overestimated because the strip sample were compressed between the upper and lower anvils in a semi-constrained condition. The material was then flown out between the anvils during compressing and during straining in the HPS facility.

The true pressure may be estimated from the following equation:[109]

$$P_c(\rho) = \frac{3}{2}\beta_0(\eta^{\frac{7}{3}} - \eta^{\frac{5}{3}})\left[1 + \frac{3}{4}(\eta^{\frac{2}{3}} - 1)(\beta'_0 - 4)\right] \quad (1)$$

where $\beta_0 = 111.0$ GPa and $\beta_0' = 3.48$ for α Ti, and $\eta = \rho/\rho_0$ is the ratio of the densities under applied and ambient pressures (ρ and ρ_0), respectively. This ratio can be equated as $\eta = (d_0/d)^3$ where d_0 and d are the lattice spacings at the corresponding conditions.

The pressures calculated using eq. (1) for the applications of 6, 7 and 8.5 GPa are shown in Fig. 10 for (a) monochromatic X-ray and (b) white X-rays. The calculation includes the pressures after straining by HPS processing. Two peaks from the α phase, $(010)_\alpha$ and $(012)_\alpha$, were used for this calculation. The following four points should be noted in association with Fig. 10.

(1) There is no significant difference in the pressure calculated using the two $(010)_\alpha$ and $(012)_\alpha$ peaks.

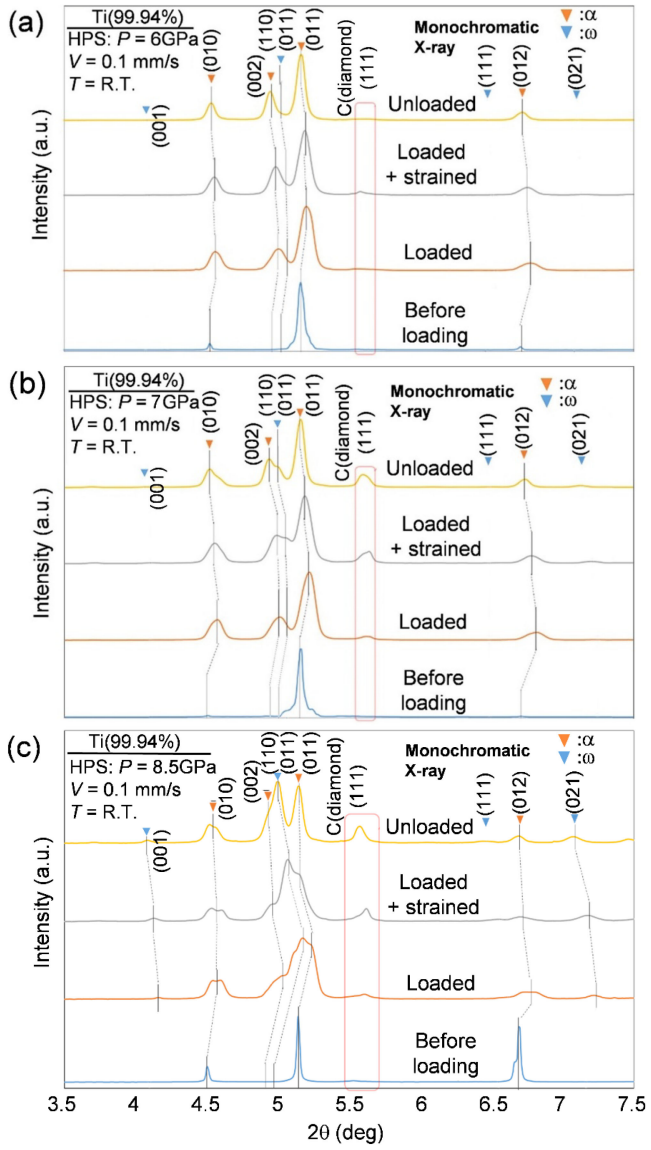

Fig. 7 Profiles acquired using monochromatic X-ray under three nominal pressures: (a) 6 GPa, (b) 7 GPa and (c) 8.5 GPa. X-ray profiles before loading, after loading, after straining by HPS processing and after releasing pressures are included.

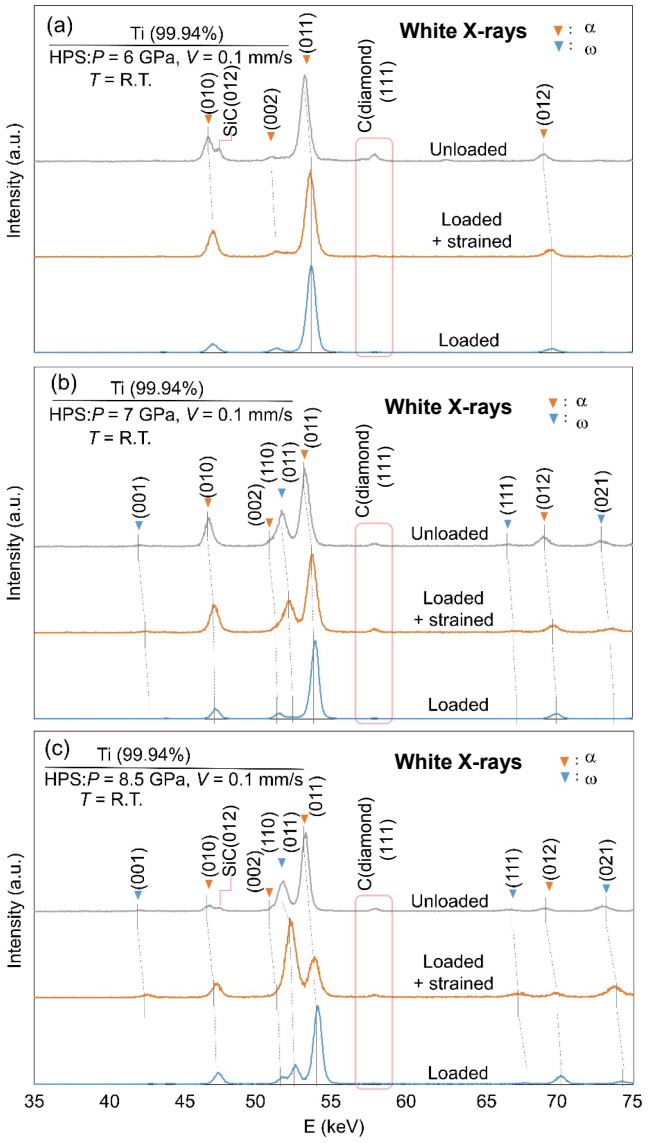

Fig. 8 Profiles acquired using white X-rays under three nominal pressures: (a) 6 GPa, (b) 7 GPa and (c) 8.5 GPa. X-ray profiles after loading, after straining by HPS processing and after releasing pressures are included.

(2) The calculated pressures are invariably lower than the applied nominal pressures, indicating that the nominal pressure derived from the load divided by the area was overestimated. It is considered that this overestimation is attributed to the overflow of the materials towards the space between the upper and lower anvils due to a semi-constrained condition. A similar overestimation was also reported for HPT processing.[110)]

(3) The nominal pressures slightly decreased upon straining by the HPS processing and this must be due to an occurrence of misalignment caused by the horizontal movement of anvils with respect to each other. This tendency is also the case for the calculated pressure, and the decrease in the calculated pressure can be caused by the decrease in the nominal pressure.

(4) The pressure calculated using the monochromatic X-ray under the nominal pressure of 8.5 GPa is significantly lowered. Referring to Fig. 7 and Fig. 8, peak broadening was prominent for the use of monochromatic X-ray especially under 8.5 GPa, while it was well reduced with the white X-rays. This is attributed to a change in camera length due to an intense overflow for the monochromatic X-ray, despite the fact that the camera length was adjusted at the mid position of the sample width using CeO_2 powders before the measurements. The white X-rays are less susceptible because only the X-rays diffracted at the mid position of the sample width were detected by the Ge-SSD through the collimator as illustrated in Fig. 4(b).

All the calculated (true) pressures are plotted against the nominal pressures in Fig. 11, where for the horizontal axis, the slight decrease in the nominal pressure upon straining by HPS processing was taken into account. The equi-line representing the nominal pressure equal to the true pressure is delineated in Fig. 11. It is apparent that the nominal pressure was overestimated (by about 1.7 times) as all data points are located below the equi-line. The overestimation appeared to

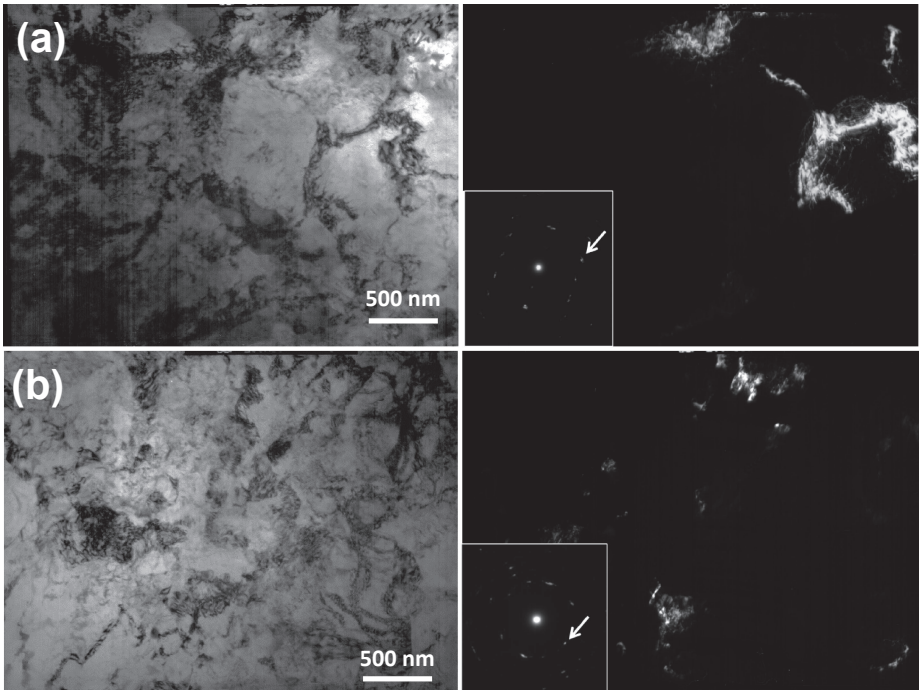

Fig. 9 TEM microstructures after HPS processing under (a) 6 GPa and (b) 8.5 GPa: bright-field images (left), dark-field images (right) and selected area electron diffraction patterns (center) with diffraction spots indicated by arrows.

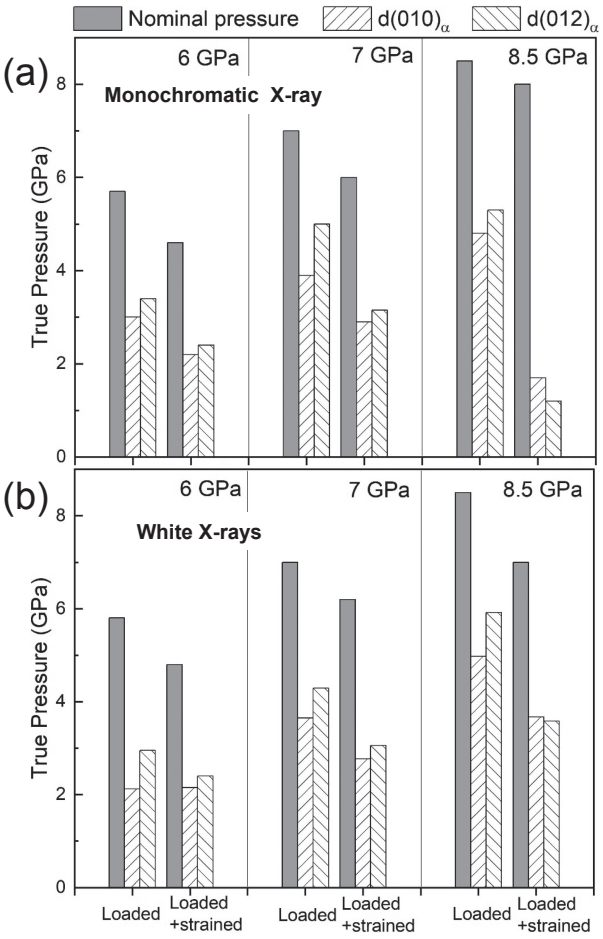

Fig. 10 Pressures calculated using lattice spacings of $d(010)_\alpha$ and $d(012)_\alpha$ for (a) monochromatic X-ray and (b) white X-rays including nominal pressures upon application of 6, 7 and 8.5 GPa and after straining by HPS processing.

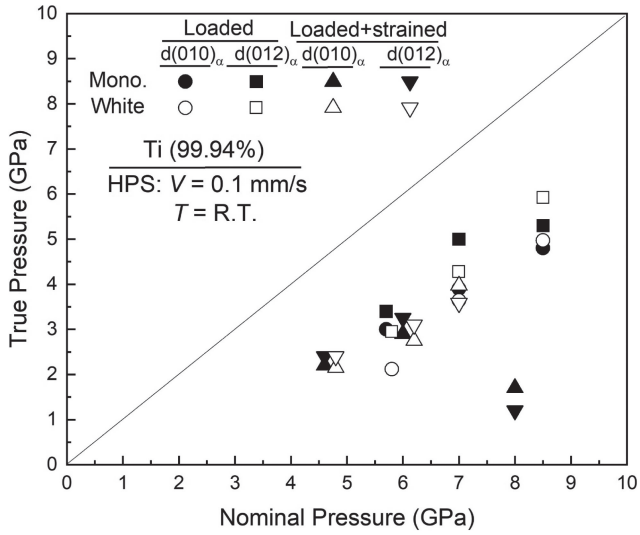

Fig. 11 Plots of true pressures calculated using X-ray peaks corresponding to $d(010)_\alpha$ and $d(012)_\alpha$ vs. nominal pressures. Slight decreases in nominal pressure are taken into account.

be more significant when the applied (nominal) pressure is lowered.

Figure 12 summarizes the results of this study with the information regarding the presence or the absence of the ω phase. It should be noted that the data points obtained under the nominal pressure of 8.5 GPa and straining are excluded in Fig. 12 because of the ambiguity involved in the measurement as mentioned above. Figure 12 includes, for reference, the phase boundary between the α phase and the ω phase drawn by Hennig *et al.*[89] When the ω phase was present, the points are marked with hatching but the marks are kept open

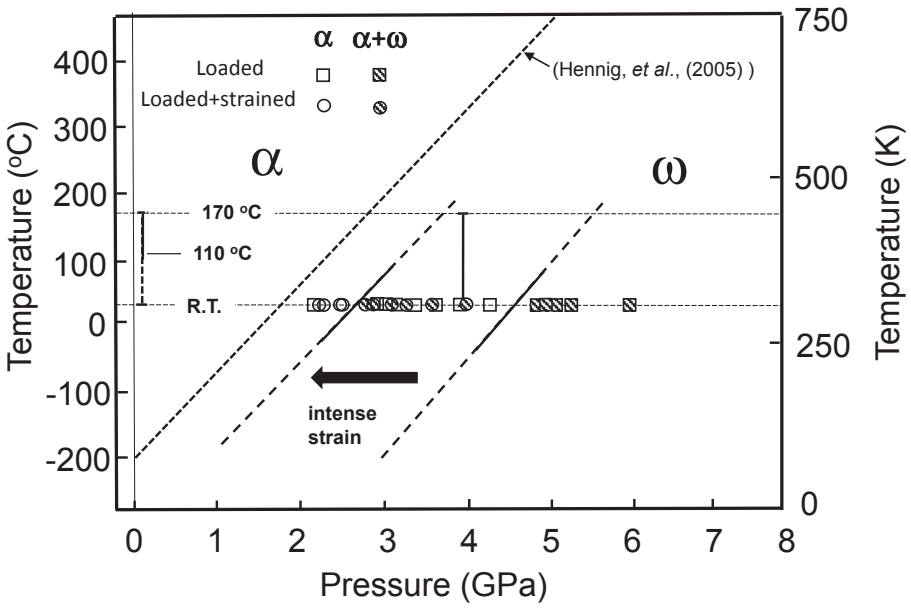

Fig. 12 Plots of true pressures presenting formation of ω phase upon loading and upon loading plus straining. Results after temperature increase under ambient pressure and application of ~4 GPa for samples containing ω phase produced by HPT processing. Phase boundary reported by Hennig *et al.*[89] is delineated.

when the ω phase was not detected. The marks are also distinguished between the cases of mere loading and loading plus intense straining using square and circular symbols, respectively. The following two points should be noted. First, the ω phase was detected after mere loading with more than ~4.5 GPa but only the α phase was detected below it. Second, the transformation pressure from the α phase to the ω phase is shifted to a lower pressure as ~2.5 GPa when the intense strain by the HPS processing is introduced. Thus, the introduction of strain assists the transformation from the α phase to the ω phase and lowers the transformation pressure. In addition, the present analysis showed that the ω phase remained exist even after unloading. Several reports are available to verify this.[96–107] Levitas reported that the strain-assisted phase transformation occurred through stress concentration due to pile-up of dislocations.[52]

Figure 12 includes the results obtained from the temperature increase under ambient pressure and the application of nominal pressure of 7 GPa which is now ~4 GPa. The ω phase produced by HPT processing transformed back to the α phase when the temperature increased to more than 110°C as shown in Fig. 5. However, under the true pressure of ~4 GPa (nominal pressure of 7 GPa), the reverse transformation from the ω phase to the α phase did not occur even as the temperature increased to 170°C as shown in Fig. 6. This is consistent with the new phase boundary determined in the present study, as depicted in Fig. 12 which indicates that the ω phase is stable in a higher temperature range including 170°C when the strain exists. However, under ambient pressure, the α phase is stable so that the transformation of the ω phase to the α phase occurred through the assistance of thermal energy. Adachi *et al.*[105] reported from electrical resistivity measurements and calorimetric measurements that the reverse transformation from the ω phase to the α phase is controlled by self-diffusion of Ti. It is considered that the stress concentration through dislocation pile-up was released by the recovery of dislocations which were acting on the ω phase to keep its crystal structures.

Importance of the *in situ* X-ray analysis is that it is possible to evaluate the true pressure so that ambiguity is less involved in the pressure measurement. As presented in this study, the pressure was overestimated because of the overflow of materials, and this is not only the case of HPS processing but also the case of the HPT processing. Furthermore, there exists a variation of pressure within the sample as simulated by Pereira and Figueiredo[111] for HPT processing. Nevertheless, it is an advantage of the *in situ* high-energy X-ray analysis that the existence of the ω phase is evaluated by the real pressure applying on the material.

5. Summary and Conclusions

This study successfully conducted *in situ* high-energy X-ray diffraction (XRD) analysis for the allotropic transformation of pure Ti using a process of high-pressure sliding (HPS). The HPS facility developed earlier for severe plastic deformation under high pressure was modified for the *in situ* high-energy XRD analysis in SPring-8. The phase transformation was examined in terms of temperature, pressure and imposed strain. The conclusions were reached as follows.

(1) The ω phase produced by high-pressure torsion under 6 GPa for 4 turns began to transform to α phase when it was heated at temperatures more than ~110°C under ambient pressure. However, when heated under a true pressure of ~4 GPa, the ω phase remained stable up to ~170°C covered in this study. These results were consistent with the pressure-temperature phase diagram in the influence of strain. The results also suggest that the reverse transformation from the ω phase to the α phase is controlled by thermal energy.

(2) The true pressure applied on the sample was estimated from the peak shift. It was found that the nominal

pressure, which was determined by the applied load divided by the initial area, was overestimated. The overestimation resulted in about 1.7 times and this was due to an overflow of the material between the upper and lower anvils in a semi-constrained condition.

(3) The overflow of the material caused a local variation of applied pressure so that peak broadening occurred. This peak broadening was reduced by the use of white X-rays.

(4) The transformation to the ω phase was promoted when strain was introduced by the HPS processing. The ω phase stays stable even after unloading when the sample was processed by HPS. The straining was effective to promote the transformation of α phase to ω phase and to maintain the ω phase even at ambient pressure. This was considered to be due to stress concentration developed through dislocation pile-up during the deformation.

(5) The advantage of the *in situ* high-energy X-ray analysis is that the phase transformation is evaluated by the true applied pressure without overestimation.

Acknowledgements

This work was supported-by a Grant-in-Aid for Scientific Research (A) from the MEXT, Japan (JP19H00830). One of the authors (TM) would like to acknowledge a Grant-in-Aid for Young Scientists from MEXT, Japan (JP19K15324). YT acknowledges the Aluminium Research Grant Program of Japan Aluminium Association. The synchrotron radiation experiments were performed at the BL04B1 of SPring-8 with the approval of the Japan Synchrotron Radiation Research Institute (JASRI) (Proposal No. 2017A1851, 2017A1864, 2017A1972, 2017B1487, 2018A1451, 2018B1494 and 2018B1697).

REFERENCES

1) K. Edalati and Z. Horita: Mater. Trans. **60** (2019) 1103.
2) Z. Horita and K. Edalati: Mater. Trans. **61** (2020) 2241–2247.
3) R.Z. Valiev, R.K. Islamgaliev and I.V. Alexandrov: Prog. Mater. Sci. **45** (2000) 103–189.
4) R.Z. Valiev, Y. Estrin, Z. Horita, T.G. Langdon, M.J. Zehetbauer and Y.T. Zhu: JOM **58**(4) (2006) 33–39.
5) R.Z. Valiev and T.G. Langdon: Prog. Mater. Sci. **51** (2006) 881–981.
6) A. Azushima, R. Kopp, A. Korhonen, D.Y. Yang, F. Micari, G.D. Lahoti, P. Groche, J. Yanagimoto, N. Tsuji, A. Rosochowski and A. Yanagida: Manuf. Technol. **57** (2008) 716–735.
7) A.P. Zhilyaev and T.G. Langdon: Prog. Mater. Sci. **53** (2008) 893–979.
8) Y. Estrin and A. Vinogradov: Acta Mater. **61** (2013) 782–817.
9) T.G. Langdon: Acta Mater. **61** (2013) 7035–7059.
10) A. Bachmaier and R. Pippan: Int. Mater. Rev. **58** (2013) 41–62.
11) R.Z. Valiev, Y. Estrin, Z. Horita, T.G. Langdon, M.J. Zehetbauer and Y.T. Zhu: Mater. Res. Lett. **4** (2016) 1–21.
12) R.Z. Valiev, Y. Estrin, Z. Horita, T.G. Langdon, M.J. Zehetbauer and Y.T. Zhu: JOM **68** (2016) 1216–1226.
13) P.W. Bridgman: Phys. Rev. **48** (1935) 825–847.
14) K. Edalati and Z. Horita: Mater. Sci. Eng. A **652** (2016) 325–352.
15) T. Masuda and Z. Horita: Mater. Trans. **60** (2019) 1104–1110.
16) S. Kuramoto and T. Furuta: Mater. Trans. **60** (2019) 1116–1122.
17) Á. Révész and Z. Kovács: Mater. Trans. **60** (2019) 1283–1293.
18) P. Kral, J. Dvorak, V. Sklenicka and T.G. Langdon: Mater. Trans. **60** (2019) 1506–1517.
19) K. Edalati, J. Matsuda, H. Iwaoka, S. Toh, E. Akiba and Z. Horita: Int. J. Hydrogen Energ. **38** (2013) 4622–4627.
20) K. Edalati, E. Akiba and Z. Horita: Sci. Technol. Adv. Mater. **19** (2018) 185–193.
21) Y. Ikoma, K. Hayano, K. Edalati, K. Saito, Q. Guo and Z. Horita: Appl. Phys. Lett. **101** (2012) 121908.
22) Y. Ikoma, K. Kumano, K. Edalati, M.R. McCartney, D.J. Smith and Z. Horita: Mater. Charact. **132** (2017) 132–138.
23) Y. Ikoma: Mater. Trans. **60** (2019) 1168–1176.
24) Y. Ikoma, T. Yamasaki, T. Shimizu, M. Takaira, M. Kohno, Q. Guo, M.R. McCartney, D.J. Smith, Y. Arai and Z. Horita: Mater. Charact. **169** (2020) 110590.
25) H. Razavi-Khosroshahi and M. Fuji: Mater. Trans. **60** (2019) 1203–1208.
26) J. Hidalgo-Jimenez, Q. Wang, K. Edalati, J.M. Cubero-Sesín, H. Razavi-Khosroshahi, Y. Ikoma, D. Gutiérrez-Fallas, F.A. Dittel-Meza, J.C. Rodríguez-Rufino, M. Fuji and Z. Horita: Int. J. Plast. **124** (2020) 170–185.
27) A.V. Korznikov, I. Safarov, D.V. Laptionok and R.Z. Valiev: Acta Metall. Mater. **39** (1991) 3193–3197.
28) H. Shen, B. Guenther, A.V. Koanikov and R.Z. Valiev: Nanostruct. Mater. **6** (1995) 385–388.
29) R.Z. Valiev, R.S. Mishra, J. Groza and A.K. Mukherjee: Scr. Mater. **34** (1996) 1443–1448.
30) A.R. Yavari, W.J. Botta, C.A.D. Rodrigues, C. Cardoso and R.Z. Valiev: Scr. Mater. **46** (2002) 711–716.
31) J. Sort, A.P. Zhilyaev, M. Zielinska, J. Nogues, S. Surinach, J. Thibault and M.D. Baro: Acta Mater. **51** (2003) 6385–6393.
32) Z. Lee, F. Zhou, R.Z. Valiev, E.J. Lavernia and S.R. Nutt: Scr. Mater. **51** (2004) 209–214.
33) J. Sort, D.C. Ile, A.P. Zhilyaev, A. Concustell, T. Czeppe, M. Stoica, S. Surinach, J. Eckert and M.D. Baro: Scr. Mater. **50** (2004) 1221–1225.
34) A.P. Zhilyaev, A.A. Gimazov, G.I. Raab and T.G. Langdon: Mater. Sci. Eng. A **486** (2008) 123–126.
35) A.P. Zhilyaev, S. Swaminathan, A.A. Gimazov, T.R. McNelley and T.G. Langdon: J. Mater. Sci. **43** (2008) 7451–7456.
36) K. Edalati, Y. Yokoyama and Z. Horita: Mater. Trans. **51** (2010) 23–26.
37) K. Edalati and Z. Horita: Scr. Mater. **63** (2010) 174–177.
38) A. Bachmaier, M. Kerber, D. Setman and R. Pippan: Acta Mater. **60** (2012) 860–871.
39) J.M. Cubero-Sesin and Z. Horita: Mater. Sci. Eng. A **558** (2012) 462–471.
40) K. Edalati, S. Toh, H. Iwaoka and Z. Horita: Acta Mater. **60** (2012) 3885–3893.
41) K. Edalati, H. Iwaoka, S. Toh, K. Sasaki and Z. Horita: Mater. Trans. **54** (2013) 1540–1548.
42) K. Edalati, S. Toh, M. Arita, M. Watanabe and Z. Horita: Appl. Phys. Lett. **102** (2013) 181902.
43) K. Edalati, T. Daio, Y. Ikoma, M. Arita and Z. Horita: Appl. Phys. Lett. **103** (2013) 034108.
44) S. Lee, K. Edalati, H. Iwaoka, Z. Horita, T. Ohtsuki, T. Ohkochi, M. Kotsugi, T. Kojima, M. Mizuguchi and K. Takanashi: Philos. Mag. Lett. **94** (2014) 639–646.
45) M. Kawasaki, B. Ahn, H.J. Lee, A.P. Zhilyaev and T.G. Langdon: J. Mater. Res. **31** (2016) 88–99.
46) K.S. Kormout, R. Pippan and A. Bachmaier: Adv. Eng. Mater. **19** (2017) 1600675.
47) N. Ibrahim, M. Peterlechner, F. Emeis, M. Wegner, S.V. Divinski and G. Wilde: Mater. Sci. Eng. A **685** (2017) 19–30.
48) M. Khajouei-Nezhad, M.H. Paydar, R. Ebrahimi, P. Jenei, P. Nagy and J. Gubicza: Mater. Sci. Eng. A **682** (2017) 501–508.
49) J.K. Han, J.I. Jang, T.G. Langdon and M. Kawasaki: Mater. Trans. **60** (2019) 1131–1138.
50) K. Edalati: Mater. Trans. **60** (2019) 1221–1229.
51) A. Bachmaier and R. Pippan: Mater. Trans. **60** (2019) 1256–1269.
52) V.I. Levitas: Mater. Trans. **60** (2019) 1294–1301.
53) A. Mazilkin, B. Straumal, A. Kilmametov, P. Straumal and B. Baretzky: Mater. Trans. **60** (2019) 1489–1499.

54) V.D. Blank, M.Y. Popov and B.A. Kulnitskiy: Mater. Trans. **60** (2019) 1500–1505.
55) T. Fujioka and Z. Horita: Mater. Trans. **50** (2009) 930–933.
56) K. Tazoe and Z. Horita: J. JILM **62** (2012) 454–458.
57) S. Lee, K. Tazoe, I.F. Mohamed and Z. Horita: Mater. Sci. Eng. A **628** (2015) 56–61.
58) Y. Takizawa, T. Masuda, K. Fujimitsu, T. Kajita, K. Watanabe, M. Yumoto, Y. Otagiri and Z. Horita: Metall. Mater. Trans. A **47** (2016) 4669–4681.
59) V. Sklenicka, P. Kral, J. Dvorak, Y. Takizawa, T. Masuda, Z. Horita, K. Kucharova, M. Kvapilova and M. Svobodova: Adv. Eng. Mater. **22** (2020) 1900448.
60) Y. Tang, T. Komatsu, T. Masuda, M. Arita, Y. Takizawa, M. Yumoto, Y. Otagiri and Z. Horita: Materialia **14** (2020) 100916.
61) T. Masuda, K. Fujimitsu, Y. Takizawa and Z. Horita: Lett. Mater. **5** (2015) 258–263.
62) T. Masuda, K. Fujimitsu, Y. Takizawa and Z. Horita: J. JILM **65** (2015) 319–325.
63) T. Masuda, K. Fujimitsu, Y. Takizawa and Z. Horita: J. Japan Inst. Metals Mater. **80** (2016) 128–133.
64) Y. Tang, K. Sumikawa, Y. Takizawa, M. Yumoto, Y. Otagiri and Z. Horita: Mater. Sci. Eng. A **748** (2019) 108–118.
65) Y. Tang, Y. Takizawa, M. Yumoto, Y. Otagiri and Z. Horita: Mater. Sci. Technol. **36** (2020) 877–886.
66) Y. Takizawa, K. Watanabe, T. Kajita, K. Sumikawa, T. Masuda, M. Yumoto, Y. Otagiri and Z. Horita: J. Japan Inst. Metals Mater. **82** (2018) 25–31.
67) Y. Takizawa, K. Sumikawa, K. Watanabe, M. Yumoto, Y. Kanai, Y. Otagiri and Z. Horita: Metall. Mater. Trans. A **49** (2018) 1830–1840.
68) Z. Horita, Y. Tang, T. Masuda and Y. Takizawa: Mater. Trans. **61** (2020) 1177–1190.
69) J. Gubicza: Mater. Trans. **60** (2019) 1230–1242.
70) J. Čížek, M. Janeček, T. Vlasák, B. Smola, O. Melikhova, R.K. Islamgaliev and S.V. Dobatkin: Mater. Trans. **60** (2019) 1533–1542.
71) N. Tsuji, R. Gholizadeh, R. Ueji, N. Kamikawa, L. Zhao, Y. Tian, Y. Bai and A. Shibata: Mater. Trans. **60** (2019) 1518–1532.
72) A.W. Lawson and T.Y. Tang: Rev. Sci. Instrum. **21** (1950) 815.
73) K.A. Goettel, H.K. Mao and P.M. Bell: Rev. Sci. Instrum. **56** (1985) 1420–1427.
74) Y. Ma, H.K. Mao, R.J. Hemley, S.A. Gramsch, G. Shen and M. Somayazulu: Rev. Sci. Instrum. **72** (2001) 1302–1305.
75) M.T. Vaughan, D.J. Weidner, Y.B. Wang, J.H. Chen, C.C. Koleda and I.C. Getting: Rev. High Pressure Sci. Technol. **7** (1998) 1520–1522.
76) J. Chen, L. Li, D. Weidner and M. Vaughan: Phys. Earth Planet. Inter. **143–144** (2004) 347–356.
77) V.D. Blank, Y.S. Konyaev, A.I. Kuznetsov and E.I. Estrin: Instrum. Exp. Tech. **27** (1984) 1240–1242.
78) V.D. Blank, M.Y. Popov and B.A. Kulnitskiy: Mater. Trans. **60** (2019) 1500–1505.
79) V.I. Levitas, Y. Ma, J. Hashemi, M. Holtz and N. Guven: J. Chem. Phys. **125** (2006) 044507.
80) R. Nomura, S. Azuma, K. Uesugi, Y. Nakashima, T. Irifune, T. Shinmei, S. Kakizawa, Y. Kojima and H. Kadobayashi: Rev. Sci. Instrum. **88** (2017) 044501.
81) Y. Wang, W.B. Durham, I.C. Gettin and D.J. Weidner: Rev. Sci. Instrum. **74** (2003) 3002.
82) T. Kawazoe, Y. Nishihara, T. Ohuchi, N. Nishiyama, Y. Higo, K. Funakoshi and T. Irifune: Am. Mineral. **96** (2011) 1665–1672.
83) E.A. Perez-Albuerne, K.F. Forsgren and H.G. Drickamer: Rev. Sci. Instrum. **35** (1964) 29.
84) Y. Nishihara, D. Tinker, T. Kawazoe, Y. Xu, Z. Jing, K.N. Matsukage and S.-i. Karato: Phys. Earth Planet. Inter. **170** (2008) 156–169.
85) T. Kawazoe, S. Karato, J. Ando, Z. Jing, K. Otsuka and J.W. Hustoft: J. Geophys. Res. **115** (2010) B08208.
86) D. Yamazaki and S.-I. Karato: Rev. Sci. Instrum. **72** (2001) 4207.
87) J. Girard, G. Amulele, R. Farla, A. Mohiuddin and S.-I. Karato: Science **351** (2016) 144.
88) A.R. Kilmametov, G. Vaughan, A.R. Yavari, A. LeMoulec, W.J. Botta and R.Z. Valiev: Mater. Sci. Eng. A **503** (2009) 10–13.
89) R.G. Hennig, D.R. Trinkle, J. Bouchet, S.G. Srinivasan, R.C. Albers and J.W. Wilkins: Nat. Mater. **4** (2005) 129–133.
90) P.W. Bridgman: Proc. Am. Acad. Arts Sci. **76** (1948) 71–87.
91) J.C. Jamieson: Science **140** (1963) 72–73.
92) V.A. Zilbershtein, G.I. Nosova and E.I. Estrin: Phys. Met. Met. **35** (1973) 128–133.
93) V.A. Zilbershtein, N.P. Chistotina, A.A. Zharov, N.S. Grishina and E.I. Estrin: Fiz. Met. Met. **39** (1975) 445–447.
94) V.V. Aksenenkov, V.D. Blank, Y.S. Konyayev, A.I. Kunzetsov and E.I. Estrin: Phys. Met. Met. **57** (1984) 159–162.
95) A.R. Kilmametov, A.V. Khristoforova, G. Wilde and R.Z. Valiev: Z. Kristallogr. Suppl. **26** (2007) 339–344.
96) Y. Ivanisenko, A. Kilmametov, H. Rosner and R.Z. Valiev: Int. J. Mater. Res. **99** (2008) 36–41.
97) Y. Todaka, J. Sasaki, T. Moto and M. Umemoto: Scr. Mater. **59** (2008) 615–618.
98) M.T. Pérez-Prado, A.A. Gimazov, O.A. Ruano, M.E. Kassner and A.P. Zhilyaev: Scr. Mater. **58** (2008) 219–222.
99) K. Edalati, E. Matsubara and Z. Horita: Metall. Mater. Trans. A **40** (2009) 2079–2086.
100) K. Edalati, Z. Horita, H. Fujiwara and K. Ameyama: Metall. Mater. Trans. A **41** (2010) 3308–3317.
101) M. Tane, Y. Okuda, Y. Todaka, H. Ogi and A. Nagakubo: Acta Mater. **61** (2013) 7543–7554.
102) K. Edalati, T. Daio, M. Arita, S. Lee, Z. Horita, A. Togo and I. Tanaka: Acta Mater. **68** (2014) 207–213.
103) M. Shirooyeh, J. Xu and T.G. Langdon: Mater. Sci. Eng. A **614** (2014) 223–231.
104) N. Adachi, Y. Todaka, H. Suzuki and M. Umemoto: Scr. Mater. **98** (2015) 1–4.
105) N. Adachi, Y. Todaka, K. Irie and M. Umemoto: J. Mater. Sci. **51** (2016) 2608–2615.
106) H. Shahmir and T.G. Langdon: Mater. Sci. Eng. A **667** (2016) 293–299.
107) R. Haraguchi, Y. Yoshimatsu, T. Nagaoka, M. Arita, K. Edalati and Z. Horita: J. Mater. Sci. **52** (2017) 6778–6788.
108) T. Katsura, K. Funakoshi, A. Kubo, N. Nishiyama, Y. Tange, Y. Sueda, T. Kubo and W. Utsumi: Phys. Earth Planet. Inter. **143–144** (2004) 497–506.
109) G.I. Kerley: SANDIA REPORT, (2003) pp. 1–35.
110) K. Edalati, D.J. Lee, T. Nagaoka, M. Arita, H.S. Kim, Z. Horita and R. Pippan: Mater. Trans. **57** (2016) 533–538.
111) P.H.R. Pereira and R.B. Figueiredo: Mater. Trans. **60** (2019) 1139–1150.